

## PARTICLE-BASED MULTISCALE MODELING OF CALCIUM PUFF DYNAMICS\*

ULRICH DOBRAMYSŁ<sup>†</sup>, STEN RÜDIGER<sup>‡</sup>, AND RADEK ERBAN<sup>†</sup>

**Abstract.** Intracellular calcium is regulated in part by the release of  $\text{Ca}^{2+}$  ions from the endoplasmic reticulum via inositol-4,5-triphosphate receptor ( $\text{IP}_3\text{R}$ ) channels (among other possibilities such as RyR and L-type calcium channels). The resulting dynamics are highly diverse and lead to local calcium “puffs” as well as global waves propagating through cells, as observed in *Xenopus* oocytes, neurons, and other cell types. Local fluctuations in the number of calcium ions play a crucial role in the onset of these features. Previous modeling studies of calcium puff dynamics stemming from  $\text{IP}_3\text{R}$  channels have predominantly focused on stochastic channel models coupled to deterministic diffusion of ions, thereby neglecting local fluctuations of the ion number. Tracking of individual ions is computationally difficult due to the scale separation in the  $\text{Ca}^{2+}$  concentration when channels are in the open or closed states. In this paper, a spatial multiscale model for investigating of the dynamics of puffs is presented. It couples Brownian motion (diffusion) of ions with a stochastic channel gating model. The model is used to analyze calcium puff statistics. Concentration time traces as well as channel state information are studied. We identify the regime in which puffs can be found and develop a mean-field theory to extract the boundary of this regime. Puffs are possible only when the time scale of channel inhibition is sufficiently large. Implications for the understanding of puff generation and termination are discussed.

**Key words.** intracellular calcium, calcium puffs, multiscale modeling, stochastic diffusion

**AMS subject classifications.** 65C35, 92C42

**DOI.** 10.1137/15M1015030

**1. Introduction.** Intracellular calcium plays a major role in many signaling pathways and regulates enzymatic activity, gene expression [7], and neural activity [60, 36]. In order to control a variety of cell functions, cells control the local cytoplasmic calcium concentration via the exchange of  $\text{Ca}^{2+}$  ions with the extracellular space and the release of  $\text{Ca}^{2+}$  ions through channels situated on the membrane of reservoirs, such as the endoplasmic and the sarcoplasmic reticulum. Modulation of the  $\text{Ca}^{2+}$  release regulates muscle contraction, pathway cross-talk, and mitochondrial activity, and disruption of these processes is associated with various diseases such as early-onset Alzheimer’s [5, 57], heart failure [3, 2], and such psychological conditions as bipolar disorder and schizophrenia [6]. Hence, detailed knowledge about the underlying processes governing this signaling mechanism is necessary for progress in our understanding of these diseases.

In this paper, we focus on the release of calcium ions from the endoplasmic reticulum (ER) via inositol-4,5-triphosphate receptor ( $\text{IP}_3\text{R}$ ) channels. Upon the binding of  $\text{Ca}^{2+}$  to binding sites on its cytosolic part, a channel opens, and calcium ions

\*Received by the editors April 1, 2015; accepted for publication (in revised form) April 8, 2016; published electronically July 21, 2016. This work was partially supported by the European Research Council under the European Community’s Seventh Framework Programme (FP7/2007–2013)/ERC grant agreement 239870.

<http://www.siam.org/journals/mms/14-3/M101503.html>

<sup>†</sup>Mathematical Institute, University of Oxford, Radcliffe Observatory Quarter, Woodstock Road, Oxford, OX2 6GG, United Kingdom (dobramysl@maths.ox.ac.uk, erban@maths.ox.ac.uk). The work of the third author was supported in part by the Royal Society through a University Research Fellowship, and by the Leverhulme Trust through a Philip Leverhulme Prize.

<sup>‡</sup>Institut für Physik, Humboldt-Universität zu Berlin, 12489 Berlin, Germany (sten.ruediger@physik.hu-berlin.de). The work of this author was supported in part by the Deutsche Forschungsgemeinschaft (RU1660 and IRTG 1740).

flow from the ER into the cytoplasm. Channels occur in clusters of 10 to 20 channels [12, 47]. The opening of a single channel usually triggers the release of  $\text{Ca}^{2+}$  from other channels in the same cluster due to the increased  $\text{Ca}^{2+}$  concentration in their vicinity [46]. This mechanism results in a highly localized increase of the cytosolic calcium concentration. These “puffs” of calcium ions have been detected and analyzed in experiments by using fluorescent calcium buffers [58, 23].

Traditional approaches to modeling intracellular calcium dynamics are based on deterministic macroscopic rate equations [27, 11]; however, the intrinsically random, erratic nature of calcium signals in many cells or cell domains necessitates an approach going beyond the deterministic regime [59, 24, 31, 44]. Progress has been made by recognizing the importance of number fluctuations in the binding to the channels [48, 18] and by using hybrid models, where the deterministic calcium concentration is coupled to stochastic channel binding models [42]. Recently, it was found that local fluctuations stemming from diffusive noise (i.e., noise originating from the random movement of ions) have a crucial influence on calcium dynamics for clusters of intracellular channels, particularly on the interpuff waiting time [22] but also on single-channel equilibrium behavior [56]. Stochastic effects were also investigated for L-type calcium channels and RyR channels in the dyadic cleft [34, 49, 28]. Other studies consider a Langevin equation governing the fraction of open channels in a cluster [54]. However, tracking the exact diffusion of individual ions in the complete computational domain is computationally intensive.

Here, for the first time, we apply spatial stochastic multiscale methods to model the dynamics of calcium puffs, including the release of  $\text{Ca}^{2+}$  from  $\text{IP}_3\text{R}$  channels, and track individual ion positions in order to accurately incorporate diffusive noise. We take into account both activating and inhibitory channel properties. We study the dynamics of the calcium concentration as a function of the ion binding affinities and explore the regime where there exist puffs, as well as the regime in which channels do not close after their first opening. The paper is organized as follows: In section 2 we discuss the spatial stochastic model for diffusion and channel gating used throughout this study. Section 3 discusses the multiscale approach that we employ in order to reduce the computational effort required to track single ions and hence make this study feasible. In section 4 we present results on the statistics of puffs extracted from simulated time series data, and study the transition between perpetually open channel clusters and the parameter regime in which puffs can be observed. In addition, we develop a mean-field model for channel dynamics and use it to extract the boundary between the regimes. Finally, we summarize our findings in section 5.

**2. Spatial stochastic model for intracellular  $\text{Ca}^{2+}$  release.** The spatial extent of our computational model consists of the three-dimensional domain  $\Omega$  which models a part of the intracellular space.  $\text{Ca}^{2+}$  ions are able to undergo free diffusion in  $\Omega$ . They bind to and dissociate from binding sites on the channels, which are positioned on a small area of the domain boundary, corresponding to the membrane of the ER. The domain geometry and boundary conditions are specified in section 2.2. In the following subsections we discuss the components of this model in detail. The parameter values used throughout this study can be found in Table 1.

**2.1. Diffusion—Brownian Dynamics.** A versatile method for the simulation of particles in a solution is given by Brownian Dynamics (BD). Collisions of particles with solution molecules lead to overdamped dynamics and random forcing on a sufficiently long time scale [15]. Assuming that there are  $Q(t)$  free ions in the simulation

TABLE 1

Parameter values for the spatial stochastic simulations, for physiologically relevant conditions [43].

Parameter description	Name	Value
Parameter values from the literature		
Free $\text{Ca}^{2+}$ diffusion constant [1]	$D$	$220 \mu\text{m}^2/\text{s}$
Cytoplasmic $\text{Ca}^{2+}$ concentration [43]	$c_0$	$0.02 \mu\text{M}$
Edge length of computational domain [43]	$L$	$5 \mu\text{m}$
Rate of binding to activating site [43]	$a_a$	$100 \mu\text{M}^{-1}\text{s}^{-1}$
Rate of unbinding from activating site [43]	$b_a$	$20 \text{s}^{-1}$
Open channel current [8, 47, 51]	$I_C$	$0.1 \text{pA}$
Number of channels in cluster [43, 12, 48]	$C$	9
Chosen simulation parameters		
Spacing between channels in cluster	$\ell$	$0.15 \mu\text{m}$
Rate of binding to inhibitory site	$a_i$	Varies
Rate of unbinding from inhibitory site	$b_i$	Varies
Binding radius	$\varrho$	$0.03 \mu\text{m}$
Unbinding radius	$\sigma$	$0.015 \mu\text{m}$
BD time step	$\Delta t$	$0.1 \text{ms}$
Edge length of BD regime	$L_{BD}$	$1 \mu\text{m}$
Compartment size	$h$	$0.2 \mu\text{m}$

domain at time  $t$ , the equation for Brownian motion of ions is given by

$$(2.1) \quad d\mathbf{X}_j = \sqrt{2D} d\mathbf{W}_j, \quad j = 1, 2, \dots, Q(t),$$

where  $D$  is the diffusion coefficient of ions in solution,  $\mathbf{X}_j(t) \in \Omega$  describes the trajectory of the  $j$ th ion, and  $\mathbf{W}_j$  is a three-dimensional vector of independent Wiener processes. This approach dramatically reduces the dimensionality of the problem compared to molecular dynamics approaches wherein the degrees of freedom of every participating molecule need to be taken into account. Nevertheless, the computational load is still high compared to deterministic PDE-based approaches to diffusion. There are a number of approaches for simulating (2.1) in the literature, ranging from discretization with a fixed time step [4] to event-based methods [52, 37]. In this paper, we discretize time with the time step  $\Delta t$  and use the Euler–Maruyama discretization of (2.1); i.e., the position of the  $j$ th ion is updated according to

$$(2.2) \quad \mathbf{X}_j(t + \Delta t) = \mathbf{X}_j(t) + \sqrt{2D\Delta t} \boldsymbol{\xi}_j, \quad j = 1, 2, \dots, Q(t),$$

where  $\boldsymbol{\xi}_j$  is a vector of three independent normally distributed random numbers with zero mean and unit variance.

**2.2. Domain geometry and boundary conditions.** In our simulations, the computational domain is given as cube  $\Omega = [0, L]^3$ , where the value of  $L$  is specified together with other parameters in Table 1.  $\text{Ca}^{2+}$  ions are able to undergo free diffusion in  $\Omega$ , which we simulate using (2.2). A cluster of nine  $\text{IP}_3\text{R}$  channels is positioned in

a  $3 \times 3$  grid with channel spacing  $\ell = 0.15 \mu\text{m}$ , centered in the  $z = 0$  plane; i.e., the positions of nine channels in the cluster are given as

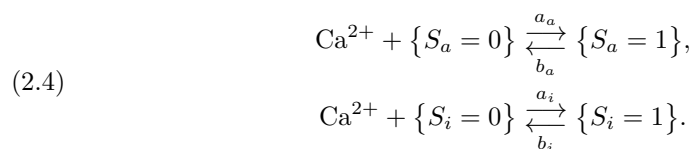
$$(2.3) \quad \left[ \frac{L}{2}, \frac{L}{2}, 0 \right], \quad \left[ \frac{L}{2} \pm \ell, \frac{L}{2}, 0 \right], \quad \left[ \frac{L}{2}, \frac{L}{2} \pm \ell, 0 \right], \quad \left[ \frac{L}{2} \pm \ell, \frac{L}{2} \pm \ell, 0 \right].$$

We found no significant effects from varying the channel spacing  $\ell$ ; hence we chose this particular cluster configuration for ease of implementation. Ions bind to and dissociate from binding sites on the channels. The boundaries of the computational domain at  $x = 0$ ,  $x = L$ ,  $y = 0$ ,  $y = L$ , and  $z = L$  are constant-concentration boundaries, and hence they absorb and introduce ions such that in the absence of open channels the concentration of  $\text{Ca}^{2+}$  in the computational domain is held at its equilibrium value,  $c_0$ , on average. Hence, ions can enter and leave the domain via the boundaries, in addition to being introduced through open channels. The boundary at  $z = 0$  is reflective, corresponding to the membrane of the ER.

If the channels are closed, then the average number of free ions in the computational domain,  $\langle Q(t) \rangle$ , is equal to  $c_0 |\Omega|$ , where  $|\Omega| = L^3$  is the volume of  $\Omega$ . Using our parameter values (see Table 1),  $c_0 |\Omega| \approx 1.5 \times 10^3$ . The average number of ions in the simulation domain,  $\langle Q(t) \rangle$ , increases when the channels are open (by around two orders of magnitude). In order to simulate the system over sufficiently long time intervals, we will use a multiscale approach, which we describe in detail in section 3.

**2.3. Stochastic channel binding model.** The conformational changes between the open and closed states of IP<sub>3</sub>R channels are controlled by the binding of  $\text{Ca}^{2+}$  to activating and inhibitory binding sites. These channels consist of four subunits, each of which can be in an active or a neutral/inhibited state. Each subunit has three different binding sites: An activating binding site for  $\text{Ca}^{2+}$  ions, an inhibitory binding site for  $\text{Ca}^{2+}$  ions, and an IP<sub>3</sub> binding site.

To accurately capture channel gating events, we employ a simplified DeYoung–Keizer model [11]. Here, we disregard IP<sub>3</sub> dynamics and consider the effects of IP<sub>3</sub> only via their influence on the dissociation constant  $b_i$  of  $\text{Ca}^{2+}$  ions from inhibitory binding sites. Free  $\text{Ca}^{2+}$  ions can bind to the activating and inhibitory sites, while bound ions can dissociate from occupied sites. Therefore, there are two reversible reactions in our model for each subunit of a channel:



The rates  $a_a$  and  $a_i$  describe the binding affinity of a  $\text{Ca}^{2+}$  ion to an activating or inhibitory binding site, respectively, while the off-rates  $b_a$  and  $b_i$  describe the corresponding dissociation reaction rates. The variables  $S_a$  and  $S_i$  describe the binding site state and can take values of 0 and 1. Channels consist of four subunits, with each subunit having one activating and one inhibitory  $\text{Ca}^{2+}$ -binding site; see Figure 1. A model subunit can then be in three distinct states: neutral (no binding site occupied), active (only the activating site occupied), and inhibited (if the inhibitory site is occupied regardless of the state of the activating site). A channel then opens when at least three of its four subunits are in the active state.

**2.4. Ion binding dynamics.** In order to precisely capture channel opening and closing dynamics, we need to implement a reversible BD binding model of  $\text{Ca}^{2+}$  ions

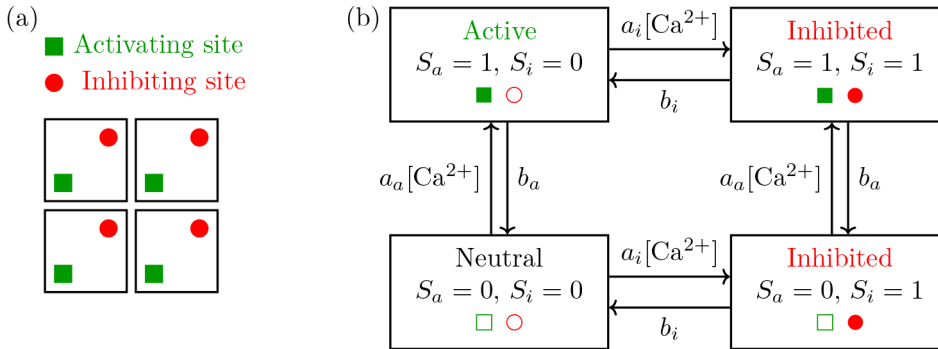


FIG. 1. (a) Sketch of a channel, containing four subunits with an activating ion binding site (green square) and an inhibiting site (red circle). (b) State space of a single subunit. Ions can bind to the activating and the inhibiting sites. A subunit is active only if it has an occupied activating site as well as an empty inhibiting site.

to their corresponding binding sites. Ions become binding candidates as soon as they enter a half-sphere of radius  $\varrho$  around a binding site. (The channels are positioned on the ER membrane, and hence only the half-sphere above them is available for ion binding.) They are then allowed to bind to the site with a probability  $P_\lambda$  per time step spent in the binding region [35, 16]. An ion bound to an activating site (resp., inhibitory site) is allowed to dissociate with a probability  $1 - \exp(-b_a \Delta t)$  (resp.,  $1 - \exp(-b_i \Delta t)$ ) and placed at a distance of  $\sigma$  (unbinding radius) from the binding site. We use the values of binding and unbinding radii,  $\varrho$  and  $\sigma$ , as given in Table 1. Their values are chosen to be reasonable, such that no overlaps occur between channels and that they are large enough such that the BD simulation time step can be chosen reasonably large. Then we can precalculate the remaining parameter  $P_\lambda$  (binding probability) before the start of simulations using the approach described in [35, section 5].

**2.5. Channel opening and calcium flux.** Each channel has four subunits. Let  $S_a^{j,k}(t) \in \{0, 1\}$  (resp.,  $S_i^{j,k}(t) \in \{0, 1\}$ ),  $j = 1, 2, \dots, 9$ ,  $k = 1, 2, 3, 4$ , be the state of the activating (resp., inhibiting) site of the  $k$ th subunit of the  $j$ th channel in the cluster. Then the number of active subunits of the  $j$ th channel at time  $t$  is

$$N_a^j(t) = \sum_{k=1}^4 S_a^{j,k}(t) (1 - S_i^{j,k}(t)).$$

If  $N_a^j(t) \geq 3$ , then the channel is considered to be in an open state. When a channel is open, new ions are introduced with a rate of  $3.12 \times 10^5 \text{ s}^{-1}$  (corresponding to channel current  $I_C = 0.1 \text{ pA}$  [8, 47, 51]) at the channel site, simulating the flux of  $\text{Ca}^{2+}$  ions out of an active channel. The positions of released ions then evolve according to (2.2).

**3. Multiscale approach.** During a puff event, a large number of ions are released into the cytoplasm. If all channels are open continuously, then one can estimate, for the parameter values given in Table 1, that our computational domain may contain on the order of  $10^5$  ions during the peak of a puff. Since we are interested in time scales of minutes, tracking the individual position of this number of ions via Brownian dynamics becomes infeasible. However, high accuracy and individual ion positions are only needed in the vicinity of channel sites in order to ensure accurate

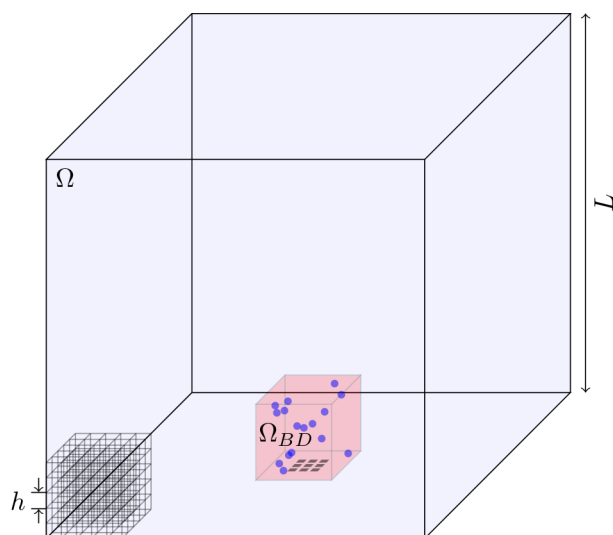


FIG. 2. Sketch of the computational domain  $\Omega$ . It consists of two regions: The compartment-based part  $\Omega \setminus \Omega_{BD}$  (everywhere except for the red box in the bottom center, with the compartment size  $h$  illustrated in the left bottom of the picture) and the BD domain  $\Omega_{BD}$  (shown as a red box in the bottom center). The boundary in both  $x$ - and  $y$ -directions as well as the boundary at  $z = L$  are constant-concentration boundaries, while the boundary at  $z = 0$  is reflective. The channel cluster is positioned at the center of the  $z = 0$  boundary (indicated as black squares); see (2.3).

implementation of BD binding dynamics, described in section 2.4. Therefore, we split our computational domain into two regions: a cube

$$\Omega_{BD} = \left[ \frac{L - L_{BD}}{2}, \frac{L + L_{BD}}{2} \right] \times \left[ \frac{L - L_{BD}}{2}, \frac{L + L_{BD}}{2} \right] \times [0, L_{BD}]$$

containing the channel sites (red region in Figure 2), as well as the remaining space  $\Omega \setminus \Omega_{BD}$  in which we will use a coarser description of ion movement, as described in the next subsection. Here,  $L_{BD} < L$  is the length of the edge of the cube  $\Omega_{BD}$ . We use  $L_{BD} = L/5$  in our simulations (see Table 1). In particular, we use BD simulations in a small fraction of  $1/5^3 \approx 0.8\%$  of the computational domain  $\Omega$ .

**3.1. Compartment-based model for diffusion.** We subdivide the region  $\Omega \setminus \Omega_{BD}$  into compartments (cubes) with size  $h$  (illustrated in the bottom left of Figure 2) and employ a compartment-based method to simulate the movement of ions [17]. Ions are allowed to move between adjacent compartments with a rate of  $d = D/h^2$ . The compartment-based algorithm stores and evolves only the number of ions in each compartment (rather than following individual ions). An event-based stochastic simulation algorithm is used to efficiently simulate this system. Several equivalent methods have been developed in the literature, such as the Gillespie algorithm [26], the Next Reaction Method [25], the Next Subvolume Method [14, 30], as well as the Optimized Direct Method [9].

In this paper, we employ the next reaction method [25]. For each possible move between two neighboring compartments, a putative time for the next jump of an ion to occur is calculated. It is given by

$$(3.1) \quad t - \frac{\ln(r)}{d A_c(t)},$$

where  $t$  is the current simulation time,  $d = D/h^2$  is the jump rate for one ion,  $A_c(t)$  is the current number of ions in the compartment from which an ion is jumping, and  $r$  is a random number uniformly distributed in the interval  $(0, 1)$ . Clearly, the putative jump time (3.1) is infinity if  $A_c(t) = 0$ , i.e., if the corresponding compartment is empty. The putative times are smaller (on average) if the corresponding compartment contains more ions.

The putative jump times are inserted into a priority queue (a heap data structure [10]), which enables us to efficiently extract the earliest jump time and thus the next jump. This move is then performed, and the numbers of ions in compartments (and the corresponding putative times and their entries in the priority queue) are updated. We then iterate this process by finding the minimal putative time and performing the corresponding ion jump at each iteration.

At the boundaries of the computational domain  $\Omega$  (except for the boundary at  $z = 0$ , which is reflective), ions are absorbed (i.e., they leave the domain) or can enter with rates consistent with a constant equilibrium concentration of  $c_0$  outside the domain. The jump rate from outside the domain into a compartment just inside the domain boundary is  $c_0 D h$ , which is used, instead of  $d A_C(t)$ , in (3.1) to compute the corresponding putative times.

**3.2. Coupling the BD simulation in  $\Omega_{BD}$  with the compartment-based approach in  $\Omega \setminus \Omega_{BD}$ .** Several methods exist in order to couple the BD and compartment-based methods across their interface, such as the two-regime method (TRM) [19, 20] or the ghost-cell method [21]. Here, we employ the TRM. In order to accurately capture diffusion across the interface, the jump rates from adjacent compartments into  $\Omega_{BD}$  need to be adjusted from the bulk rate  $d = D/h^2$  to the interface rate [19]

$$(3.2) \quad d_i = \frac{2}{h} \sqrt{\frac{D}{\pi \Delta t}}.$$

These jump rates are used, instead of  $d$ , in (3.1) to compute the corresponding putative times. If the chosen move in the compartment regime is a jump from a compartment adjacent to the interface into  $\Omega_{BD}$ , the occupancy number of the compartment is reduced by one, and a new ion is added in  $\Omega_{BD}$  at the distance  $x$  from the interface which is sampled from the probability distribution [19]

$$(3.3) \quad f(x) = \sqrt{\frac{\pi}{4D\Delta t}} \operatorname{erfc} \left[ \frac{x}{\sqrt{4D\Delta t}} \right],$$

where  $\operatorname{erfc}$  is the complementary error function.

The rate (3.2) and the distribution (3.3) are used to transfer ions from  $\Omega \setminus \Omega_{BD}$  into  $\Omega_{BD}$ . In the opposite direction, the TRM transfers any ion from  $\Omega_{BD}$  which during the time step interacts with the interface. For a detailed discussion and the derivation of the probabilities and jump rates above, please see references [19, 20, 21]. We employ the particle-based simulation library package *Tyche*, which implements the TRM [38]. The TRM has also been recently implemented in Smoldyn [39].

**4. Results.** Simulations were performed with the parameter values listed in Table 1 unless noted differently. In section 4.1, we discuss  $\text{Ca}^{2+}$  puff statistics from simulation runs. We follow this by investigating the regimes in which puffs are visible in section 4.2. A simple mean-field theory is then presented in section 4.3. It describes the transition between puffs and perpetually open channels.

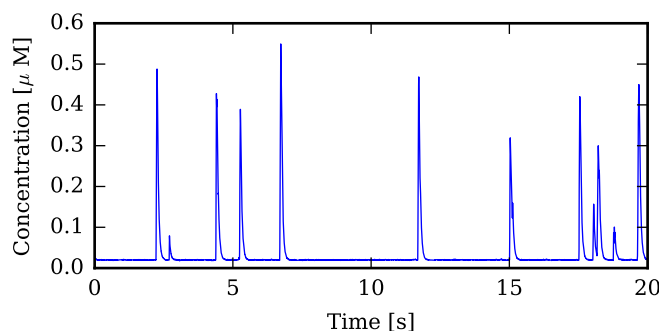


FIG. 3. Example concentration time trace for  $a_i = 1 \mu\text{M}^{-1}\text{s}^{-1}$  and  $b_i = 1 \text{s}^{-1}$ .

**4.1. Puff statistics.** Figure 3 displays a sample time trace of the  $\text{Ca}^{2+}$  concentration in the computational domain for  $a_i = 1 \mu\text{M}^{-1}\text{s}^{-1}$  and  $b_i = 1 \text{s}^{-1}$  for a time range of 20 s. The ion concentration shows erratic calcium puffs with an amplitude of up to  $0.5 \mu\text{M}$ . The constant background of  $c_0 = 0.02 \mu\text{M}$  corresponds to approximately 12 ions per  $\mu\text{m}^3$  and justifies our use of BD because fluctuations in such a small number of ions influence binding to the channels. The puffs are characterized by a sharp, almost instant, increase in concentration, followed by an approximately exponential decay after the channel cluster closes. Puffs are separated by a refractory phase in which channel subunits are inhibited and the cluster cannot open.

We analyze the concentration data given as the time values  $t_j$  and concentration values  $c_j$ ,  $j = 1, 2, \dots, N$  (where  $N$  is the index of the last data point of the simulation run), by choosing a puff-starting threshold concentration value

$$(4.1) \quad c_t = \langle c_j \rangle + \sqrt{\text{Var}[c_j]},$$

i.e., one standard deviation above the mean concentration  $\langle c_j \rangle$ . For the data set shown below, the threshold was  $c_t \approx 0.1 \mu\text{M}$ . The averaging in (4.1) is taken over all values of  $j$ ,  $j = 1, 2, \dots, N$ ; i.e., the sample mean and variance in (4.1) are estimated by

$$(4.2) \quad \langle c_j \rangle = \frac{1}{N} \sum_{j=1}^N c_j \quad \text{and} \quad \text{Var}[c_j] = \frac{1}{N-1} \sum_{j=1}^N (c_j - \langle c_j \rangle)^2.$$

Puffs are identified by the concentration crossing the threshold point (4.1). Puff ending points are identified via a recrossing of this value. The crossing points are given in the ordered index set

$$\mathcal{S} = \{j \mid c_{j-1} < c_t \text{ and } c_j \geq c_t, j = 2, 3, \dots, N\}$$

(puff starting indices) and

$$\mathcal{E} = \{j \mid c_j > c_t \text{ and } c_{j+1} \leq c_t, j = 1, 2, 3, \dots, N-1\}$$

(puff ending indices). The sets  $\mathcal{S}$  and  $\mathcal{E}$  are enumerated by the puff index  $1 \leq k \leq N_p$ , where  $N_p = |\mathcal{E}|$  is the number of finished puffs in the data set; i.e., we disregard the last index in  $\mathcal{S}$  if the last puff did not finish and denote

$$\mathcal{S} = \{s_1, s_2, \dots, s_{N_p}\} \quad \text{and} \quad \mathcal{E} = \{e_1, e_2, \dots, e_{N_p}\},$$



where the elements in  $\mathcal{S}$  (resp.,  $\mathcal{E}$ ) are ordered, i.e.,  $s_1 < s_2 < \dots < s_{N_p}$  (resp.,  $e_1 < e_2 < \dots < e_{N_p}$ ). The interpuff times are then given by

$$(4.3) \quad \mathcal{T} = \left\{ t_{s_{k+1}} - t_{e_k} \mid s_{k+1} \in \mathcal{S}, e_k \in \mathcal{E}, 1 \leq k \leq N_p - 1 \right\} \cap (t_p, \infty),$$

where the threshold  $t_p = 0.25$  s. This threshold filtering decreases the number of puffs considered by removing the puffs which are not well separated. Indeed, the inset in Figure 4(a) shows that the distribution of interpuff times below the threshold follows an exponential distribution and is due to random channel reopenings stemming from residual calcium. The distribution of interpuff times (histogram of set  $\mathcal{T}$ ) is shown in Figure 4(a) for a set of 954 puff intervals. Its shape is similar to a Gamma distribution:

$$(4.4) \quad p(\tau) = \frac{1}{\Gamma(\kappa)\theta^\kappa} \tau^{\kappa-1} e^{-\tau/\theta}.$$

Indeed, when choosing  $\kappa = 2.82$  and  $\theta = 0.64$  s in (4.4) (such that the resulting distribution has the same mean and variance as our data), the comparison is good. As the Erlang distribution (the special case of a Gamma distribution with  $\kappa \in \mathbb{N}$ ) results from summing  $\kappa$  exponentially distributed random variables, we can speculate that an effective model of calcium channel opening might be described by a three-stage binding/unbinding process. The maximum of the interpuff time distribution,  $\tau_m \approx 1.81$  s, can be interpreted as the typical time between puffs in this system.

The distribution of puff amplitudes is determined by taking the maximum value in a previously determined puff interval,

$$\mathcal{A} = \left\{ a_k \mid a_k = \max_{s_k \leq j \leq e_k} c_j, \text{ where } s_k \in \mathcal{S}, e_k \in \mathcal{E}, 1 \leq k \leq N_p \right\}.$$

The amplitude distribution (histogram of set  $\mathcal{A}$ ) is shown in Figure 4(b) and mirrors the broad distribution characterized in experiments [13].

The puff durations are calculated by considering the full duration at half maximum, which is a common criterion for determining the puff duration in the literature [13]. To this end, we calculate the indices of crossings of the half maximum threshold on the rising slope of a puff,

$$\mathcal{R} = \left\{ r_k \mid r_k = \max \left\{ j \mid c_{j-1} < \frac{a_k}{2} \text{ and } c_j \geq \frac{a_k}{2} \text{ and } s_k \leq j \leq e_k \right\}, \right. \\ \left. \text{where } s_k \in \mathcal{S}, e_k \in \mathcal{E}, a_k \in \mathcal{A}, 1 \leq k \leq N_p \right\},$$

and the falling slope of a puff,

$$\mathcal{F} = \left\{ f_k \mid f_k = \min \left\{ j \mid c_j > \frac{a_k}{2} \text{ and } c_{j+1} \leq \frac{a_k}{2} \text{ and } s_k \leq j \leq e_k \right\}, \right. \\ \left. \text{where } s_k \in \mathcal{S}, e_k \in \mathcal{E}, a_k \in \mathcal{A}, 1 \leq k \leq N_p \right\}.$$

The puff durations are then calculated via

$$\mathcal{D} = \{ t_{f_k} - t_{r_k} \mid f_k \in \mathcal{F}, r_k \in \mathcal{R}, 1 \leq k \leq N_p \}.$$

The distribution of puff durations (histogram of set  $\mathcal{D}$ ) is plotted in Figure 4(c). The distribution is sharply peaked around 0.03 s and has a long tail stemming from

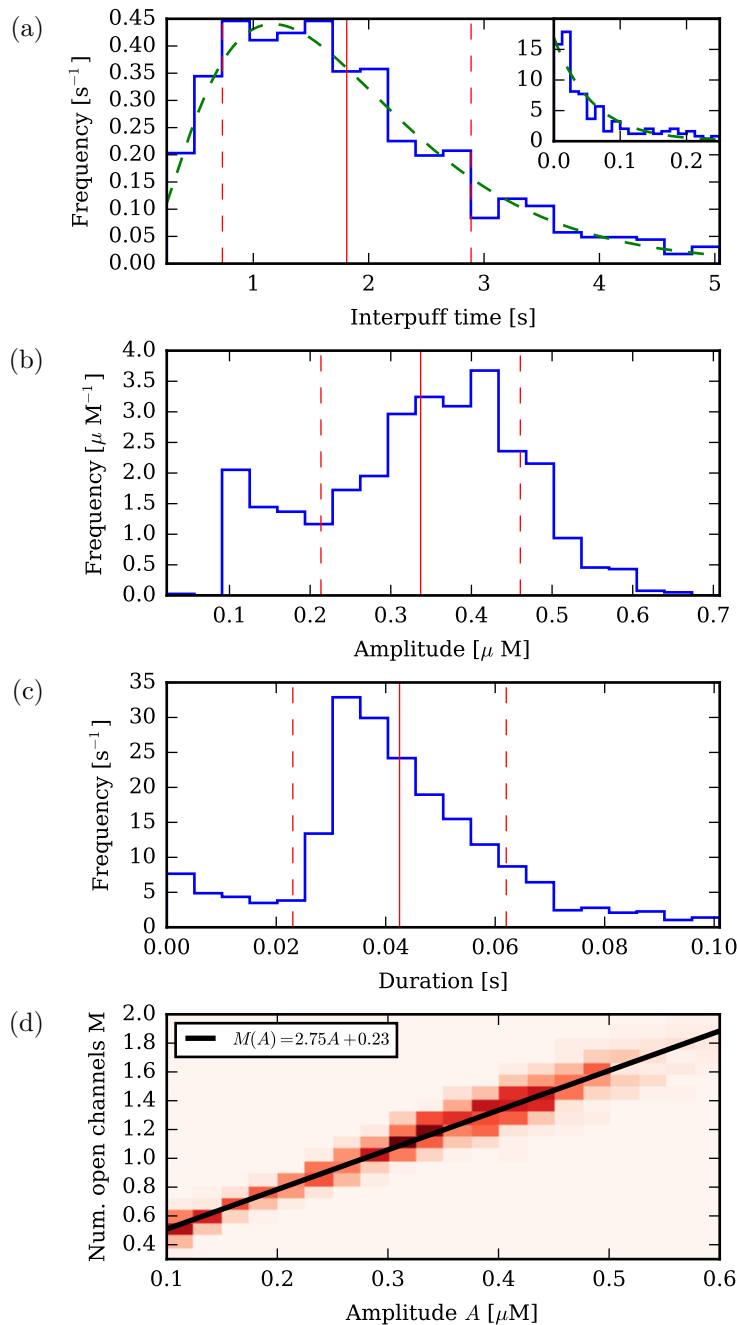


FIG. 4. Calcium puff statistics for a set of  $N_p = 1151$  puffs from simulations with a total duration of 3 simulation hours. The mean and standard deviations of the distributions are indicated by the solid and dashed red (vertical) lines, respectively. (a) Interpuff time distribution for 545 puff intervals after threshold filtering (4.3). The mean interpuff time is  $1.81 \pm 1.077$  s. The green dashed curve displays Gamma distribution (4.4) with  $\kappa = 2.82$  and  $\theta = 0.64$  s. The inset shows the distribution of interpuff times smaller than 250 ms with a mean of  $0.59 \pm 0.061$  s. (b) Amplitude distribution. The mean puff amplitude is  $0.34 \pm 0.12$  μM (indicated by the red vertical lines). (c) Puff duration (full duration at half amplitude) distribution. The mean puff duration is  $0.04 \pm 0.02$  s. (d) A two-dimensional histogram showing the strong correlation between the average number of open channels (over a puff's duration) and the puff amplitude. The black line indicates a linear fit to the correlation data.

repeated cluster reopenings during the concentration decay phase. The mean puff lifetime is within the range 40–70 ms measured in experiments [13].

Figure 4(d) displays the correlation between the number of open channels averaged over a puff's duration  $M$  and the puff amplitude  $A$ . By finding the average  $M(A)$  for each value of  $A$  and performing a linear fit, we find the linear relationship  $M(A) = 2.75 \mu\text{M}^{-1}A + 0.23$ .

**4.2. Inhibition transition.** Figure 5 shows the results of a simulation run with two different values of inhibitory site dissociation rate  $b_i$ , illustrating two different modes of behavior. We use the same value of  $a_i$  in all four panels; the rest of the parameter values are given in Table 1. Figures 5(a)–(b) show the results of a simulation run with  $b_i = 5 \text{ s}^{-1}$  (corresponding to a dissociation constant of  $K_D = b_i/a_i = 50 \mu\text{M}$ ). These simulation parameters are consistent with the modeling of calcium puffs in the literature and are used in hybrid PDE-based models [43]. Figure 5(a) shows the  $\text{Ca}^{2+}$  concentration in the computational domain  $\Omega$ , while Figure 5(b) displays the fraction of occupied inhibitory sites in the channel cluster as a function of time. Due to the large dissociation rate, the necessary level of bound inhibitory sites can never be sustained long enough for all the channels in the cluster to close at the same time. Therefore, the  $\text{Ca}^{2+}$  concentration is kept at a level where empty activating sites are immediately filled and the channel cluster stays perpetually open. Hence, puff termination in this case can be speculated to be facilitated by a mechanism other than channel inhibition, such as ER  $\text{Ca}^{2+}$  reservoir depletion or a mechanism involving dissociation of  $\text{IP}_3$  [40]. We checked the influence of lowering the binding radius  $\varrho$  to 6 nm and found that it had no effect on the channel cluster closing.

In contrast, a lower inhibitory site dissociation constant yields well-defined calcium puffs in our particle-based simulation scheme. Figures 5(c)–(d) display data from simulation runs with  $b_i = 0.1 \text{ s}^{-1}$  (which corresponds to  $K_D = b_i/a_i = 1 \mu\text{M}$ ). Here, inhibitory site binding is sustained on a high level for a long enough time such that all channels close and the excess  $\text{Ca}^{2+}$  is removed. Hence there are time intervals when the concentration of  $\text{Ca}^{2+}$  near clusters decreases and reaches the equilibrium  $\text{Ca}^{2+}$  concentration  $c_0$ . Puffs are therefore clearly delineated and separated with a well-defined interpuff time.

Hence there exist two regimes: a puff regime (Figures 5(c) and 5(d)) and a regime with perpetually open channel clusters (Figures 5(a) and 5(b)). We now proceed to characterize concentration and open channel time traces to find under which conditions well-defined puffs are possible. To this end, we use the “puff score” characterization function introduced in [29], which quantifies the spike-ness of a given time trace of the number of open channels. We denote the number of open channels at time point  $t_j$  by  $O_j$ ,  $j = 1, 2, \dots, N$ , i.e.,  $O_j \in \{0, 1, 2, \dots, C\}$ , where  $C = 9$  in our simulations. Then the puff score is defined by

$$(4.5) \quad [\text{PS}](a_i, b_i) = \frac{1}{C} \frac{\text{Var}[O_j]}{\langle O_j \rangle},$$

where the averages are again take over all values of  $j$ ,  $j = 1, 2, \dots, N$  (compare with (4.2)). The puff score (4.5) can take values in  $[0, 1]$ . A puff score greater than 0.25 indicates channel excitability and therefore the existence of puffs in the system.

In order to visualize the two parameter regimes, we performed simulations for different inhibitory site binding parameters  $a_i \in [0.1, 1] \mu\text{M}^{-1}\text{s}^{-1}$  and  $b_i \in [1, 10] \text{ s}^{-1}$  for a simulation time duration of 100 s. We extracted the number of open channels over time and calculated the puff score (4.5). Figure 6 displays this quantity. The

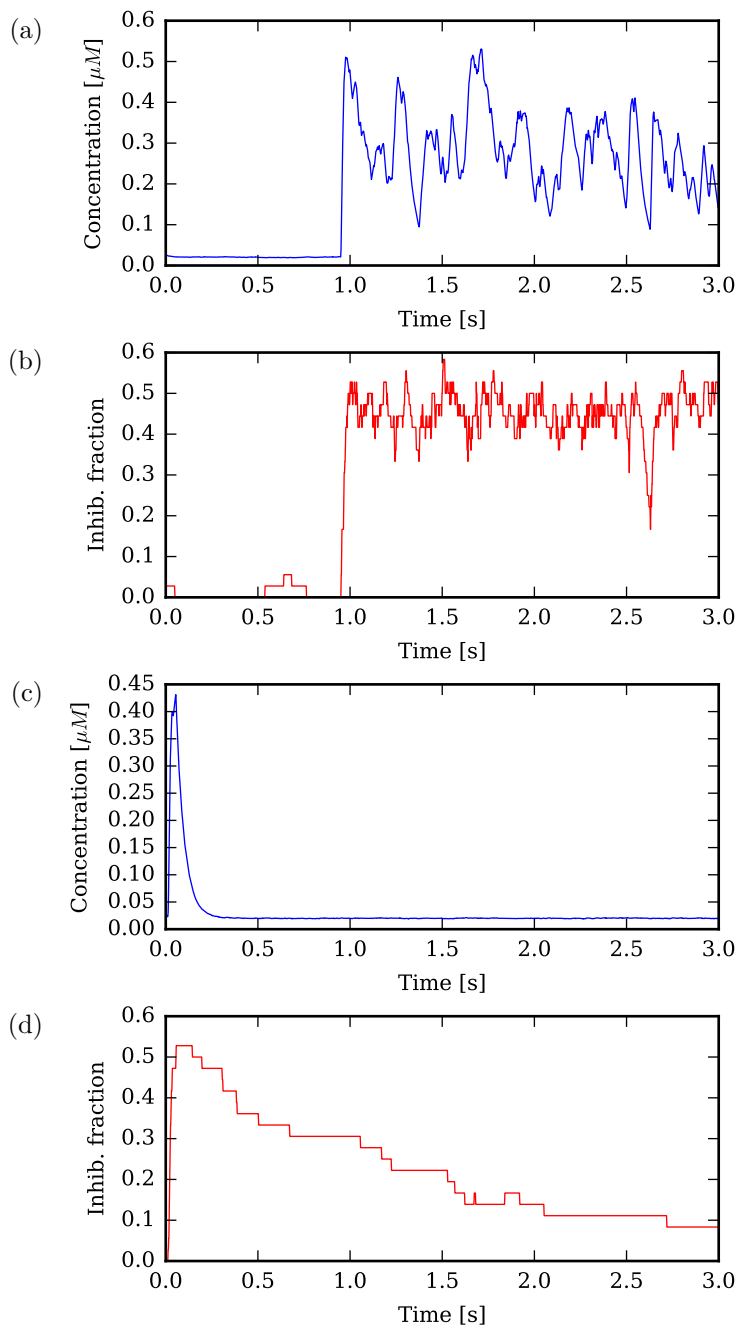


FIG. 5. (a) Calcium concentration and (b) fraction of inhibited channel subunits as a function of time for  $a_i = 0.1 \mu\text{M}^{-1}\text{s}^{-1}$  and  $b_i = 5 \text{s}^{-1}$ . Other parameter values are given in Table 1. Note that the channel cluster stays perpetually active in this configuration. (c)  $\text{Ca}^{2+}$  concentration and (d) fraction of occupied inhibitory binding sites in the channel cluster as a function of time for the inhibitory site binding parameters  $a_i = 0.1 \mu\text{M}^{-1}\text{s}^{-1}$  and  $b_i = 0.1 \text{s}^{-1}$ . Other parameter values are given in Table 1. Note that the time scale of inhibition decay is long enough for the calcium concentration to decay completely; thus the channel cluster closes and we can identify well-defined puffs.

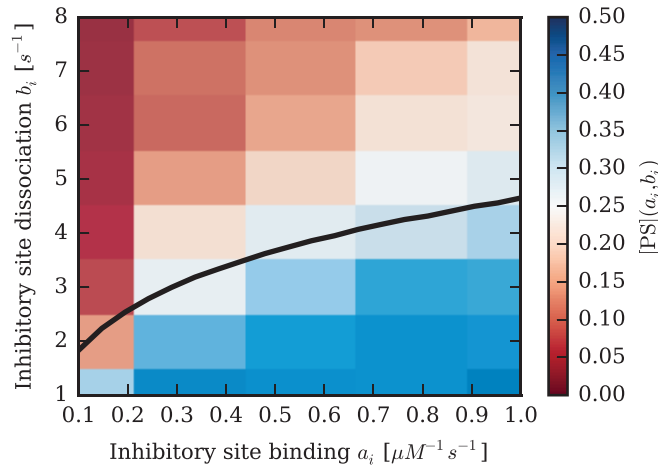


FIG. 6. Phase plot of  $a_i$  and  $b_i$ . Color indicates the puff score (4.5) for the set of parameters listed in Table 1. The black line shows the numerically determined phase boundary from the mean-field model (4.6)–(4.8).

color indicates the value of  $[\text{PS}](a_i, b_i)$ . The transition between the two regimes is not sharp, but gradual, especially for higher  $a_i$ . This is due to prolonged channel reopenings becoming more likely due to faster dissociation of bound inhibiting ions when  $b_i$  approaches the transition. The phase boundary is consistent with a dissociation constant of  $4 \mu\text{M} < K_D < 10 \mu\text{M}$ .

To directly compare our results with previously used schemes from the literature, we devised a simplified hybrid scheme: The main difference between our method and hybrid simulation algorithms is the much lower calcium concentration in the vicinity of open channels and the resulting weaker channel inhibition. Therefore, in the simplified hybrid scheme, whenever a channel is open, we do not use the particle-based binding described in section 2.4. Instead we assume a constant high calcium concentration of  $c_B = 150 \mu\text{M}$  (consistent with results from hybrid simulations [43]) to generate random binding events to inhibitory sites with a rate of  $a_i c_B$ , irrespective of any ions in the vicinity. In all other respects, the simulation proceeds as described previously. Figure 7 shows the resulting map of puff scores.

In order to study the influence of buffers (whose main effect is to slow down ion diffusion [33]) on the boundary of the puff regime, we performed a similar set of simulations with a lower  $\text{Ca}^{2+}$  diffusion constant of  $D = 20 \mu\text{m}^2/\text{s}$ . Because ions bound to buffer molecules can be viewed as slowly diffusing ions, lowering the diffusion constant is a way to model the effects of buffers [53]. The result is shown in Figure 8. With a lower diffusion constant, the calcium concentration in the channel cluster nanodomains decays more slowly. For puffs to exist, the time scale of the decay of inhibitory site binding needs to be longer than the time scale of  $\text{Ca}^{2+}$  decay. Hence, the boundary separating the two regimes is pushed to smaller values of the inhibitory dissociation rate  $b_i$ , corresponding to approximately  $1 \mu\text{M} < K_D < 2 \mu\text{M}$ . Hence, the effective diffusion constant plays an important role in determining the boundary between the two regimes. Note that the overall variation of the puff score  $[\text{PS}](a_i, b_i)$  here is smaller compared to the case of  $D = 220 \mu\text{m}^2/\text{s}$ ; therefore  $\text{Ca}^{2+}$  puffs become less pronounced with slower ion diffusion.  $\text{Ca}^{2+}$  buffers lead to additional extrinsic

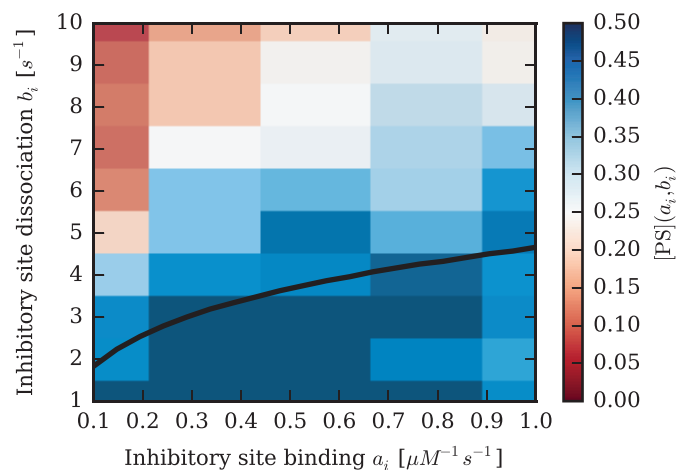


FIG. 7. Phase plot of  $a_i$  and  $b_i$  for the hybrid scheme described in the text. Color indicates the puff score (4.5) for the set of parameters listed in Table 1. For comparison, the black line shows the numerically determined phase boundary from the mean-field model (4.6)–(4.8) for Figure 6.

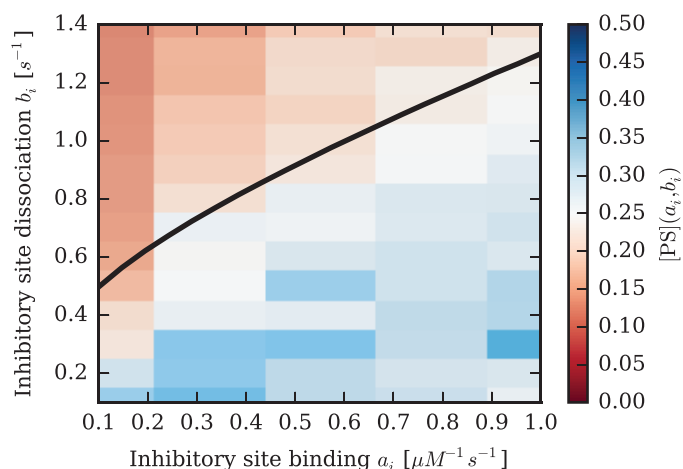


FIG. 8. Phase plot of  $a_i$  and  $b_i$  with a low diffusion constant  $D = 20 \mu\text{m}^2/\text{s}$ . The other parameters are given in Table 1. Color indicates the puff score (4.5). The black line shows the numerically determined phase boundary from the mean-field model (4.6)–(4.8). Note that the scale of the y-axis here is different from that in Figures 6 and 7.

noise due to the binding and unbinding of calcium ions to buffer molecules, which enhances  $\text{Ca}^{2+}$  fluctuations, which might have effects on the puff statistics in addition to what we have presented here [55].

**4.3. Mean-field model.** In order to find an approximate phase diagram to determine the parameter regimes in which calcium puffs occur, we develop a simplified nonspatial model. To this end, we consider an ensemble of identical channels that interact by a shared calcium domain (all-to-all coupling). The concentration  $c(t)$  in the  $1 \mu\text{m}^3$  cube around a channel undergoes exponential decay with a phenomenological

decay parameter  $\lambda$  due to diffusive equilibration, and a linear increase with an ion influx rate  $\nu$  when the channel is open. The open states of the ensemble of channels are determined by the mean number of occupied activating and inhibitory binding sites per channel,  $a(t)$  and  $b(t)$ , in a similar way as in the spatial model above. In a simple representation of the subunit dynamics and their binding cooperativity we require that a channel be open at a given time  $t$  if  $a(t) > 3$  and  $b(t) < 2$ . Here the variables  $a(t)$  and  $b(t)$  describe how many subunits, on average, have activating and inhibitory ions bound to their respective binding sites. They evolve according to the mass-action rate equations corresponding to the reactions (2.4). Hence the model equations are

$$(4.6) \quad \frac{dc}{dt} = \Theta(a-3) \Theta(2-b) \nu - \lambda(c - c_0),$$

$$(4.7) \quad \frac{da}{dt} = a_a c(4-a) - b_a a,$$

$$(4.8) \quad \frac{db}{dt} = a_i c(4-b) - b_i b.$$

Here,  $\Theta(x)$  is the Heaviside function with the properties

$$\Theta(x) = \begin{cases} 0 & \text{for } x < 0, \\ \frac{1}{2} & \text{for } x = 0, \\ 1 & \text{for } x > 0. \end{cases}$$

The first term on the right-hand side of (4.6) describes the above-mentioned channel openings: The channels open only if three subunits are active and not inhibited. The influx rate is determined via the channel current  $\nu = (2eV)^{-1}I_C = 518.28 \mu\text{M s}^{-1}$  (where  $e = 1.602 \times 10^{-19} \text{ C}$  is the electron charge; the in-flowing ions are assumed to be spread over a volume of  $V = 1 \mu\text{m}^3$ ). This value is also consistent with influx rates extracted from the rising flanks of puffs in our simulations. The exponential decay parameter  $\lambda$  was determined by fitting an exponential decay to calcium puff simulation data. The parameters of the mean-field model are summarized in Table 2.

TABLE 2  
Parameter values for the ODE mean-field model (4.6)–(4.8).

$c_0$	$0.02 \mu\text{M}$	Background $\text{Ca}^{2+}$
$\nu$	$5.18 \times 10^2 \mu\text{M s}^{-1}$	Source rate
$\lambda$	$22.9 \text{ s}^{-1}$ ( $D = 220 \mu\text{m}^2/\text{s}$ ) $2.2 \text{ s}^{-1}$ ( $D = 20 \mu\text{m}^2/\text{s}$ )	$\text{Ca}^{2+}$ decay
$a_a$	$100 \mu\text{M}^{-1} \text{ s}^{-1}$	Rate of activating site binding
$b_a$	$20 \text{ s}^{-1}$	Rate of activating site unbinding
$a_i$	$[0.1, 1] \mu\text{M}^{-1} \text{ s}^{-1}$	Rate of inhibiting site binding
$b_i$	$[0.1, 8] \text{ s}^{-1}$	Rate of inhibiting site unbinding

Figure 9 shows data from three representative numerical solutions of the ODE system (4.6)–(4.8), where the inhibitory binding rate is set to  $a_i = 0.5 \mu\text{M}^{-1} \text{ s}^{-1}$ . The initial conditions are  $c(0) = c_0$ ,  $a(0) = 4$ , and  $b(0) = 0$ . The concentration  $c(t)$  in Figure 9(a) shows a puff with its characteristic exponential decay to  $c_0$ . For  $b_i = 2 \text{ s}^{-1}$ ,

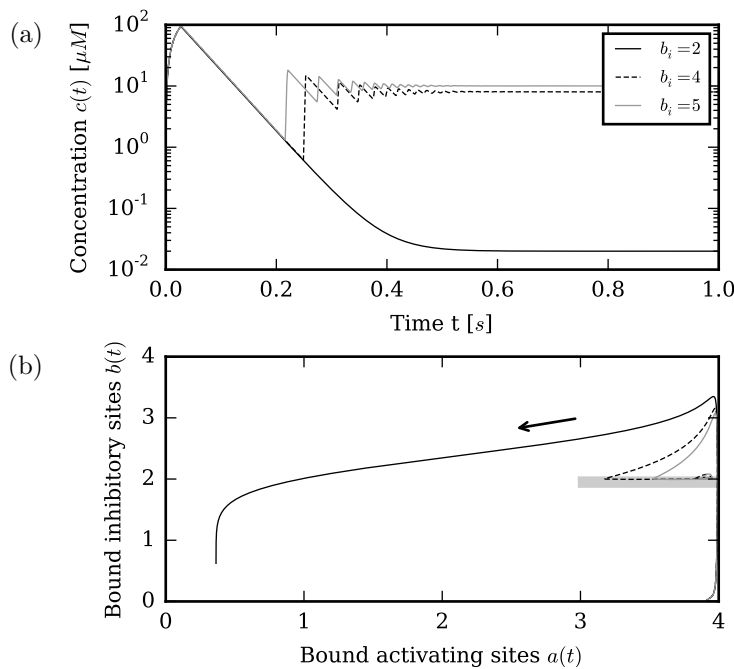


FIG. 9. (a) Concentration over time and (b) phase space trajectories of the mean-field system (4.6)–(4.8). The ratchet-like oscillation visible in the concentration traces for  $b_i = 4 \text{ s}^{-1}$  and  $5 \text{ s}^{-1}$  stems from the channels being reactivated repeatedly due to insufficient inhibition.

$c(t)$  returns to its equilibrium value  $c_0$ , while for higher values, it oscillates at a high concentration level. These two states correspond to the “puff” regime and the “always open” regime, respectively. Figure 9(b) shows the corresponding trajectories in  $a(t)$ - $b(t)$  space. When the trajectory, after its initial transient phase, does not touch the line segment  $\{(a, 2) \text{ for } a \in (3, 4)\}$ , highlighted in gray in Figure 9(b), the concentration will decay to  $c_0$  and the system returns to its original state. If, however, the  $a(t)$ - $b(t)$  trajectory hits this boundary, the system stays excited, and the channels stay perpetually open. This can be translated into a temporal criterion by viewing the time evolution of the system as a two-step process: (1) Find the time  $\tau$  such that  $b(\tau) = 2$  (i.e., the time until the second Heaviside function in (4.6) becomes zero); (2) find  $\tau_1 > \tau$  such that  $b(\tau_1) = 2$ , and  $\tau_2 > \tau$  such that  $a(\tau_2) = 3$ . If  $\tau_2 < \tau_1$ , well-defined puffs are possible; otherwise,  $c(t)$  stays elevated and channels stay perpetually open.

We now proceed to find the mean-field phase boundary between the “puff” regime and the “perpetually open” regime. Steady-state analysis of (4.6)–(4.8) does not yield the correct results in the latter regime due to the discontinuous nature of the Heaviside functions in (4.6) and the resulting temporal criterion above. The system rapidly switches between the inhibited state with  $b(t) > 2$  and the noninhibited state with  $b(t) < 2$ , leading to the observed decaying oscillations of  $c(t)$  in Figure 9(a). Hence, we numerically integrate (4.6)–(4.8) to test whether a given parameter set  $a_i, b_i$  falls into one of the two regimes. We let the system first evolve until  $b > 2$  and continue until either  $a(t)$  becomes smaller than 3 or  $b(t)$  becomes smaller than 2. We then identify the regime the system is in according to the criterion described above. A bisection algorithm is used to find the boundary  $b_i(a_i)$  between the two regimes.



The black lines in Figures 6, 7, and 8 show the extracted phase boundaries for the parameter values given in Table 2.

**5. Conclusions.** In this paper, we have reported a novel application of a particle-based spatial algorithm for diffusion to investigate the influence of diffusive noise on the dynamics of intracellular calcium release. Particle number noise in calcium microdomains has attracted interest in recent studies [22, 55, 56, 32], also for L-type and RyR calcium channels [34, 49, 28], and it is important to clarify whether calcium diffusion as an additional noise source needs to be incorporated to obtain a better understanding of subcellular calcium signals.

In order to make this study feasible, we split the domain into a compartment-based regime and a Brownian dynamics regime, coupled via the TRM. This allowed us to model the dynamics of full puffs, including release of a realistic number of ions and inhibition dynamics. We extracted concentration time traces and analyzed the resulting puff statistics. The interpuff time distribution as well as the distributions of puff amplitudes and lifetimes agree qualitatively with experimental data in the literature [23].

We then proceeded to analyze the binding parameter regimes under which well-defined  $\text{Ca}^{2+}$  puffs are possible. We found that, surprisingly, an inhibitory binding site dissociation constant  $K_D = 50 \mu\text{M}$ , consistent with the literature and patch-clamp experiments [45], does not yield puffs in our model. In this parameter regime, channels stay perpetually open. In order to investigate the transition between well-defined puffs and perpetually open channels, we characterized calcium concentration traces for various combinations of the inhibitory site binding parameters. The phase boundary visible in our data is consistent with a dissociation constant in the region  $4 \mu\text{M} < K_D < 10 \mu\text{M}$ . Lower values of the  $\text{Ca}^{2+}$  diffusion constant yield a phase boundary at smaller inhibitory site dissociation rates and thus an even smaller dissociation constant. Given the reliable puff generation and termination in previous studies based on fitted gating models with large  $K_D$  [43, 50], this is an unexpected result.

Why does our model not show the same robust termination at large  $K_D$  as the hybrid approaches [41, 43, 44]? In the latter models the binding and unbinding to the receptors is stochastic, but the calcium distribution is calculated from deterministic reaction-diffusion equations. To test for the differences of puffs in both models we have performed a set of simulations using large local  $\text{Ca}^{2+}$  concentrations for open channels, similar to what is obtained in the hybrid method. These simulations confirm the robust termination in the hybrid scheme even at large  $K_D$ . In a hybrid approach, a deep inhibitory state is achieved owing to the large local nanodomain around each open channel displayed in the solution of deterministic calcium equations [41]. Thus, in the hybrid model, a channel is not inhibited by shared calcium in the domain but by its own released calcium. This effect has been termed self-inhibition [50].

In our simulations at large  $K_D$ , however, there is insufficient inhibition of the channels during the early phase of a puff. This means that no or perhaps only one subunit per channel binds inhibitory calcium, while reliable inhibition requires binding of three or four calcium ions. Our results suggest that diffusive noise mixes calcium in the cluster domain and diminishes the localized domains around open channels and self-inhibition. Thus we are led to a model of  $\text{Ca}^{2+}$  puffs that is very different from the previous hybrid model. Our diffusive model allows inhibition only from a much less localized concentration profile and can therefore only be achieved at a much smaller dissociation constant of inhibitory binding sites. This conclusion is also supported by the mean-field ODE model that we have devised and that captures the average

binding state of the cluster's activating and inhibitory sites as well as the resulting  $\text{Ca}^{2+}$  concentration in a shared and well-mixed microdomain. This model displays a sharp phase boundary between the two regimes, which agrees well with the data from our spatial simulations.

Evidence for an inhomogeneous or homogeneous calcium distribution in the cluster is hard to obtain directly from our simulations because of the short lifetime of nanodomains. In any case, our study highlights the role of the local calcium concentration in the termination of puffs and shows that puffs are very sensitive to fluctuations of residual calcium remaining after channel closing. It has to be noted though, that, apart from the diffusive noise, there are other differences between the current BD setup and the former hybrid approaches. Notably, these include the presence of calcium-binding buffers and the effect of the terms describing the reuptake of  $\text{Ca}^{2+}$  into the ER [43], and it remains to analyze the extent to which these differences affect puff termination.

#### REFERENCES

- [1] N. L. ALLBRITTON, T. MEYER, AND L. STRYER, *Range of messenger action of calcium ion and inositol 1,4,5-trisphosphate*, Science, 258 (1992), pp. 1812–1815.
- [2] M. E. ANDERSON, *Three ways to die suddenly: Do they all require calcium calmodulin-dependent protein kinase II?*, Trans. Amer. Clinical Climatolog. Assoc., 125 (2014), pp. 173–185.
- [3] M. E. ANDERSON, J. H. BROWN, AND D. M. BERS, *CaMKII in myocardial hypertrophy and heart failure*, J. Molec. Cell. Cardiol., 51 (2011), pp. 468–473.
- [4] S. ANDREWS AND D. BRAY, *Stochastic simulation of chemical reactions with spatial resolution and single molecule detail*, Phys. Biol., 1 (2004), pp. 137–151.
- [5] M. J. BERRIDGE, *Calcium signalling and Alzheimer's disease*, Neurochem. Res., 36 (2011), pp. 1149–1156.
- [6] M. J. BERRIDGE, *Calcium signalling and psychiatric disease: Bipolar disorder and schizophrenia*, Cell Tissue Res., 357 (2014), pp. 477–492.
- [7] M. J. BERRIDGE, P. LIPP, AND M. D. BOOTMAN, *The versatility and universality of calcium signalling*, Nat. Rev. Mol. Cell Biol., 1 (2000), pp. 11–21.
- [8] L. BRUNO, G. SOLOVEY, A. C. VENTURA, S. DARGAN, AND S. P. DAWSON, *Quantifying calcium fluxes underlying calcium puffs in Xenopus laevis oocytes*, Cell Calcium, 47 (2010), pp. 273–286.
- [9] Y. CAO, H. LI, AND L. PETZOLD, *Efficient formulation of the stochastic simulation algorithm for chemically reacting systems*, J. Chem. Phys., 121 (2004), pp. 4059–4067.
- [10] T. H. CORMEN, C. E. LEISERSON, R. L. RIVEST, AND C. STEIN, *Introduction to Algorithms*, 3rd ed., MIT Press, Cambridge, MA, 2009.
- [11] G. W. DE YOUNG AND J. KEIZER, *A single-pool inositol 1,4,5-trisphosphate-receptor-based model for agonist-stimulated oscillations in  $\text{Ca}^{2+}$  concentration*, Proc. Natl. Acad. Sci. USA, 89 (1992), pp. 9895–9899.
- [12] G. D. DICKINSON, D. SWAMINATHAN, AND I. PARKER, *The probability of triggering calcium puffs is linearly related to the number of inositol trisphosphate receptors in a cluster*, Biophys. J., 102 (2012), pp. 1826–1836.
- [13] G. D. DICKINSON AND I. PARKER, *Factors determining the recruitment of inositol trisphosphate receptor channels during calcium puffs*, Biophys. J., 105 (2013), pp. 2474–2484.
- [14] J. ELF AND M. EHRENBERG, *Spontaneous separation of bi-stable biochemical systems into spatial domains of opposite phases*, Syst. Biol., 1 (2004), pp. 230–236.
- [15] R. ERBAN, *From molecular dynamics to Brownian dynamics*, Proc. Roy. Soc. A, 470 (2014), 20140036.
- [16] R. ERBAN AND S. J. CHAPMAN, *Stochastic modelling of reaction-diffusion processes: Algorithms for bimolecular reactions*, Phys. Biol., 6 (2009), 046001.

- [17] R. ERBAN, S. J. CHAPMAN, AND P. MAINI, *A Practical Guide to Stochastic Simulations of Reaction-Diffusion Processes*, preprint, <http://arxiv.org/abs/0704.1908>, 2007.
- [18] M. FALCKE, *On the role of stochastic channel behavior in intracellular  $\text{Ca}^{2+}$  dynamics*, Biophys. J., 84 (2003), pp. 42–56.
- [19] M. B. FLEGG, S. J. CHAPMAN, AND R. ERBAN, *The two-regime method for optimizing stochastic reaction-diffusion simulations*, J. Roy. Soc. Interface, 9 (2012), pp. 859–868.
- [20] M. B. FLEGG, S. J. CHAPMAN, L. ZHENG, AND R. ERBAN, *Analysis of the two-regime method on square meshes*, SIAM J. Sci. Comput., 36 (2014), pp. B561–B588.
- [21] M. B. FLEGG, S. HELLANDER, AND R. ERBAN, *Convergence of methods for coupling of microscopic and mesoscopic reaction-diffusion simulations*, J. Comput. Phys., 289 (2015), pp. 1–17.
- [22] M. B. FLEGG, S. RÜDIGER, AND R. ERBAN, *Diffusive spatio-temporal noise in a first-passage time model for intracellular calcium release*, J. Chem. Phys., 138 (2013), 154103.
- [23] D. FRAIMAN, B. PANDO, S. DARGAN, I. PARKER, AND S. P. DAWSON, *Analysis of puff dynamics in oocytes: Interdependence of puff amplitude and interpuff interval*, Biophys. J., 90 (2006), pp. 3897–3907.
- [24] K. M. FRANKS AND T. J. SEJNOWSKI, *Complexity of calcium signaling in synaptic spines*, BioEssays, 24 (2002), pp. 1130–1144.
- [25] M. A. GIBSON AND J. BRUCK, *Efficient exact stochastic simulation of chemical systems with many species and many channels*, J. Phys. Chem. A, 104 (2000), pp. 1876–1889.
- [26] D. T. GILLESPIE, *A general method for numerically simulating the stochastic time evolution of coupled chemical reactions*, J. Comput. Phys., 22 (1976), pp. 403–434.
- [27] A. GOLDBETER, G. DUPONT, AND M. J. BERRIDGE, *Minimal model for signal-induced  $\text{Ca}^{2+}$  oscillations and for their frequency encoding through protein phosphorylation*, Proc. Natl. Acad. Sci. USA, 87 (1990), pp. 1461–1465.
- [28] J. HAKE AND G. T. LINES, *Stochastic binding of  $\text{Ca}^{2+}$  ions in the dyadic cleft; Continuous versus random walk description of diffusion*, Biophys. J., 94 (2008), pp. 4184–4201.
- [29] Y. HAO, P. KEMPER, AND G. D. SMITH, *Reduction of calcium release site models via fast/slow analysis and iterative aggregation/disaggregation*, Chaos, 19 (2009), pp. 1–13.
- [30] J. HATTNE, D. FANGE, AND J. ELF, *Stochastic reaction-diffusion simulation with MesoRD*, Bioinformatics, 21 (2005), pp. 2923–2924.
- [31] D. HOLCMAN, E. KORKOTIAN, AND M. SEGAL, *Calcium dynamics in dendritic spines, modeling and experiments*, Cell Calcium, 37 (2005), pp. 467–475.
- [32] H. JI, Y. LI, AND S. H. WEINBERG, *Calcium ion fluctuations alter channel gating in a stochastic luminal calcium release site model*, IEEE/ACM Trans. Comput. Biol. Bioinform., PP (2015), pp. 1–9.
- [33] J. KEENER AND J. SNEED, *Mathematical Physiology I: Cellular Physiology*, 2nd ed., Springer, New York, 2009.
- [34] X. KOH, B. SRINIVASAN, H. S. CHING, AND A. LEVCHENKO, *A 3D Monte Carlo analysis of the role of dyadic space geometry in spark generation*, Biophys. J., 90 (2006), pp. 1999–2014.
- [35] J. LIPKOVÁ, K. C. ZYGALAKIS, S. J. CHAPMAN, AND R. ERBAN, *Analysis of Brownian dynamics simulations of reversible bimolecular reactions*, SIAM J. Appl. Math., 71 (2011), pp. 714–730.
- [36] E. NEHER AND T. SAKABA, *Multiple roles of calcium ions in the regulation of neurotransmitter release*, Neuron, 59 (2008), pp. 861–872.
- [37] T. OPPELSTRUP, V. BULATOV, A. DONEV, M. KALOS, G. GILMER, AND B. SADIGH, *First-passage kinetic Monte Carlo method*, Phys. Rev. E, 80 (2009), 066701.
- [38] M. ROBINSON, *Tyche: A multiscale stochastic reaction-diffusion modeling software library in C++ and Python*, 2013, <http://tycheSSA.github.com>.
- [39] M. ROBINSON, S. ANDREWS, AND R. ERBAN, *Multiscale reaction-diffusion simulations with Smoldyn*, Bioinformatics, 31 (2015), pp. 2406–2408.
- [40] S. RÜDIGER, P. JUNG, AND J.-W. SHUAI, *Termination of  $\text{Ca}^{2+}$  release for clustered  $\text{ip}3\text{r}$  channels*, PLoS Comput. Biol., 8 (2012), e1002485.
- [41] S. RÜDIGER, C. NAGAIHA, G. WARNECKE, AND J. SHUAI, *Calcium domains around single and clustered  $\text{IP}_3$  receptors and their modulation by buffers*, Biophys. J., 99 (2010), pp. 3–12.
- [42] S. RÜDIGER, J. SHUAI, W. HUISINGA, C. NAGAIHA, G. WARNECKE, I. PARKER, AND M. FALCKE, *Hybrid stochastic and deterministic simulations of calcium blips*, Biophys. J., 93 (2007), pp. 1847–1857.
- [43] S. RÜDIGER, J. W. SHUAI, AND I. M. SOKOLOV, *Law of mass action, detailed balance, and the modeling of calcium puffs*, Phys. Rev. Lett., 105 (2010), 048103.
- [44] S. RÜDIGER, *Stochastic models of intracellular calcium signals*, Phys. Rep., 534 (2014), pp. 39–87.

- [45] J. W. SHUAI, D. P. YANG, J. E. PEARSON, AND S. RÜDIGER, *An investigation of models of the  $IP_3R$  channel in *Xenopus* oocyte*, *Chaos*, 19 (2009), 037105.
- [46] G. D. SMITH, L. DAI, R. M. MIURA, AND A. SHERMAN, *Asymptotic analysis of buffered calcium diffusion near a point source*, *SIAM J. Appl. Math.*, 61 (2001), pp. 1816–1838.
- [47] I. F. SMITH AND I. PARKER, *Imaging the quantal substructure of single  $IP_3R$  channel activity during  $Ca^{2+}$  puffs in intact mammalian cells*, *Proc. Natl. Acad. Sci. USA*, 106 (2009), pp. 6404–6409.
- [48] S. SWILLENS, G. DUPONT, L. COMBETTES, AND P. CHAMPEIL, *From calcium blips to calcium puffs: Theoretical analysis of the requirements for interchannel communication*, *Proc. Natl. Acad. Sci. USA*, 96 (1999), pp. 13750–13755.
- [49] A. J. TANSKANEN, J. L. GREENSTEIN, A. CHEN, S. X. SUN, AND R. L. WINSLOW, *Protein geometry and placement in the cardiac dyad influence macroscopic properties of calcium-induced calcium release*, *Biophys. J.*, 92 (2007), pp. 3379–3396.
- [50] G. ULLAH, I. PARKER, D.-O. D. MAK, AND J. E. PEARSON, *Multi-scale data-driven modeling and observation of calcium puffs*, *Cell Calcium*, 52 (2012), pp. 152–160.
- [51] H. VAIS, J. K. FOSKETT, AND D.-O. D. MAK, *Unitary  $Ca(2+)$  current through recombinant type 3  $InsP(3)$  receptor channels under physiological ionic conditions*, *J. Gen. Physiol.*, 136 (2010), pp. 687–700.
- [52] J. VAN ZON AND P. TEN WOLDE, *Green's-function reaction dynamics: A particle-based approach for simulating biochemical networks in time and space*, *J. Chem. Phys.*, 123 (2005), 234910.
- [53] J. WAGNER AND J. KEIZER, *Effects of rapid buffers on  $Ca^{2+}$  diffusion and  $Ca^{2+}$  oscillations*, *Biophys. J.*, 67 (1994), pp. 447–456.
- [54] X. WANG, Y. HAO, S. H. WEINBERG, AND G. D. SMITH,  *$Ca^{2+}$ -activation kinetics modulate successive puff/spark amplitude, duration and inter-event-interval correlations in a Langevin model of stochastic  $Ca^{2+}$  release*, *Math. Biosci.*, 264 (2015), pp. 101–107.
- [55] S. H. WEINBERG AND G. D. SMITH, *The influence of  $Ca^{2+}$  buffers on free  $[Ca^{2+}]$  fluctuations and the effective volume of  $Ca^{2+}$  microdomains*, *Biophys. J.*, 106 (2014), pp. 2693–2709.
- [56] N. WIEDER, R. FINK, AND F. VON WEGNER, *Exact stochastic simulation of a calcium microdomain reveals the impact of  $Ca^{2+}$  fluctuations on  $IP_3R$  gating*, *Biophys. J.*, 108 (2015), pp. 557–567.
- [57] N. K. WOODS AND J. PADMANABHAN, *Neuronal calcium signaling and Alzheimer's disease*, *Adv. Exper. Med. Biol.*, 740 (2012), pp. 1193–1217.
- [58] Y. YAO, J. CHOI, AND I. PARKER, *Quantal puffs of intracellular  $Ca^{2+}$  evoked by inositol trisphosphate in *Xenopus* oocytes*, *J. Physiol.*, 482 (1995), pp. 533–553.
- [59] S. ZENG AND W. R. HOLMES, *The effect of noise on CaMKII activation in a dendritic spine during LTP induction*, *J. Neurophysiol.*, 103 (2010), pp. 1798–1808.
- [60] R. S. ZUCKER AND W. G. REGEHR, *Short-term synaptic plasticity*, *Annu. Rev. Physiol.*, 64 (2002), pp. 355–405.